Finite element modeling of residual stress and geometrical error formations in selective laser melting of metals

Bruna Rosso, C.; Mergheim, J.; Previtali, B.

Finite Element Modeling of residual stress and geometrical error formations in SLM of metals

Claire Bruna-Rosso[a], Julia Mergheim[b], Barbara Previtali[a]

Abstract

Recent works, both numerical and experimental, on residual stress and geometrical errors in SLM-produced parts highlighted the preponderance of these phenomena. However their mechanisms of appearance are not yet fully explained. An in-house finite element model (FEM) was developed and implemented to reproduce their formations. The consistence of the model with existing simulation results and with respect to experimental observations was checked. Simulations were then performed using a computational design of experiments to better comprehend the underlying phenomena and the influence of the laser speed and power. Relationships between process parameters and residual stress, plastic strain and geometrical errors formations have been put into evidence which can support optimization procedures at design stage.

Keywords: Selective Laser Melting, Finite Element Modeling, Thermo-mechanical model, Residual stress, Geometrical errors

1 Introduction

Despite the recent interest in the Selective Laser Melting (SLM) technology and the growing number of studies published on this topic, defects of thermo-mechanical nature are still not fully addressed [1]. One of these defects, distortions, i.e. the deformation of the part due thermal stress release, is still being intensely discussed, [2, 3, 4, 5, 6]. These macro-scale distortions are related to the stresses that develop between layers and grow throughout the part build-up [7]. However, having remaining compressive stress after the part is separated from its substrate may as well have desirable effects such as increasing the part life [8]. It is thus of interest to investigate the formation of these stresses in order to become able to control them at design stage and maintain them at non-detrimental levels and orientations [9].

Another typical defect observed in SLM-built part, and more specifically in small structure, is the discrepancy between nominal and as-built geometries. Demir & Previtali [10] reported that SLM-processed stent struts were consistently thicker than their designed dimensions which can prove to be very detrimental on their functionality [11]. That is why the final dimensions of the processed area were studied to characterize the discrepancies between nominal and actual final geometries.

The classical approach to deal with the SLM mechanical modeling at macro-scale is based on the small-strain assumption, i.e. the strains are considered small enough to neglect the effects of the geometry deformation during the process. This assumption simplifies the mechanical problem zeroing quantities that represents the stress dependence on the configuration. To the authors' knowledge, a large majority mechanical solvers previously developed for SLM simulations used this small strain approach. Indeed, these references include part-scale models, i.e. of dimensions of few centimeters. The displacements involved being of few hundreds microns (see for example [2] & [12]), considering them as infinitesimal is adapted and allows considerable computational savings.

[a]Dipartimento di Meccanica, Politecnico di Milano, Via la Masa 1, 20156 Milan, Italy

[b]Institute of Applied Mechanics, Friedrich-Alexander-Universität Erlangen-Nürnberg, Egerlandstr. 5, 91058 Erlangen, Germany

However, Ganeriwala et al. recently utilized a finite deformation algorithm for part-scale additive manufacturing of Ti-6Al-4V simulation [13]. It shows encouraging results in terms of residual stress predictions. Moreover considering the size of the present models (few millimeters), the small strain assumption did not appear valid anymore. Indeed, these deformations can hardly be considered as infinitesimal at mm-scale. That is why, unlike most of the previously developed mechanical solver for SLM simulation, a finite strain approach was adopted, that did not neglect the geometrical nonlinearities.

Considering its relative novelty, the model development technology is thoroughly described in a first section. Then the model numerical validation and consistency verification with respect to experimentally observed phenomena are introduced. It is followed by the model utilization to characterize the influence of two major process parameters (laser power P and laser speed v) on the thermo-mechanical behavior of SLM-process metals. This characterization was performed using AISI316L stainless steel, since the thermal part of the solver was experimentally validated for this material [14]. Moreover, being a widely used metal, its mechanical property are rather well documented. Finally, the computational design of experiment that was put into use and the related parametric analysis are presented together with the main results they brought.

2 Methods

2.1 Modeling approach

The thermo-mechanical model is weakly coupled, meaning that the temperature influences the mechanical variables, but the displacements do not have an impact on the thermal field. This translates into a staggered resolution that is illustrated figure 1. More specifically, the mechanical solver uses at each time step the thermal field and levels of fusion that are computed by the thermal one, presented in a previous publication [14]. For that reason, solely the mechanical aspect of the model will be introduced here.
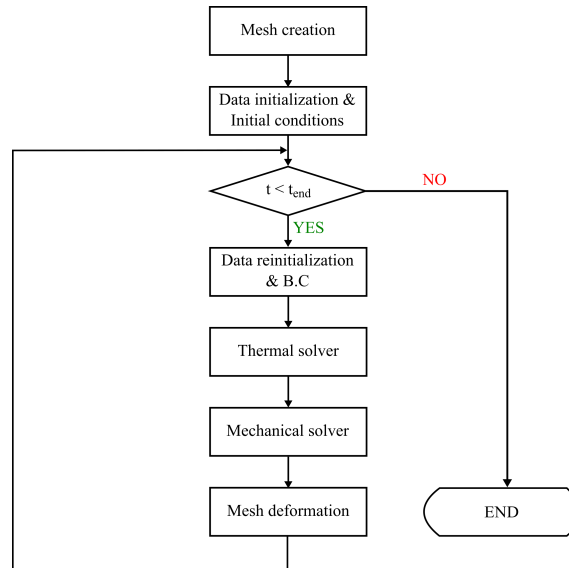

Figure 1: Thermo-mechanical simulation flowchart

Two phenomena were assumed to have a significant effect on the part mechanical behavior and will thus be represented in the model:

1. The powder shrinkage to consolidated material

2. The stress produced by the thermal gradients

The first one was included for three main motives:

- address the "mass creation" issue in the thermal model. Indeed during the phase change powder $\rightarrow$ consolidated material, the density at a node evolves from the one of the powder to the one of the bulk material. However the volume is kept constant since the mesh is fixed which lead to artificial and not-physical mass creation.

- Quantify the real dimensions of the part with respect to the input file specifications.

- Consider the deformed element geometry to compute the stress.

The second phenomenon was modeled because the stresses induced by the thermal deformations are the main responsible of the distortions observed at macro level. It is thus of great interest to study how the process creates and influences them.

2.2 Kinematic and Kinetic approaches

This subsection will explain the kinematic and kinetic approaches adopted for the description of the phenomena experienced by the material during the SLM process.

2.2.1 Multiplicative split of the deformation gradient

The approach chosen to tackle the finite strain FE simulation of the SLM process is the multiplicative split of the deformation gradient. It was put into use to derive a model that takes into account the major phenomena creating stress and strain in SLM-processed metals. The decomposition that was adopted is developed in equation 1 and is illustrated in red in figure 2.
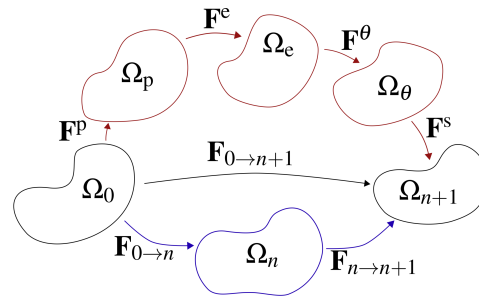
Temperature - Shrinkage - Plastic - Elastic deformation gradient decomposition
Updated Lagrange formulation deformation gradient decomposition

Figure 2: Mechanical model kinematics (red path) and formulation (blue path)

$$\mathbf{F} = \mathbf{F}^{\mathrm{p}}\mathbf{F}^{\mathrm{e}}\mathbf{F}^{\mathrm{s}}\mathbf{F}^{\theta} \tag{1}$$

Where each term $\mathbf{F}^{\bullet}$ represents a component of the total deformation gradient $\mathbf{F} = \frac{\partial \mathbf{x}}{\partial \mathbf{X}}$ produced by the various mechanical phenomena to which the material is subjected to. The computation of the different components of this decomposition will be detailed in the following sections.

2.2.2 Elasto-viscoplastic deformations

As explained in [15] the viscous phenomena begin to arise at roughly one third of the material melting temperature. Considering that in the SLM process the metal is fully melted, these effects have to be taken into account. Moreover, from a more computational point of view, using a viscoplasticity scheme is more general, numerically more stable, and the rate-independent case can be dealt with as a limit case [16]. SLM-processed metals endure elevated thermal gradients due to the local heating of the laser, as well as extreme heating/cooling rates due to the laser high energy density. It is substantially probable that these phenomena would lead to stress levels that will exceed the material yield stress. Plasticity thus has to be included in the stress state computations.

In line with these considerations, the metal behavior will be modeled using a visco-hyperelastic-plastic constitutive model. To fully define such model, three functions have to be specified: the strain energy density $\boldsymbol{\psi}$, the flow rule (also called yield criterion) f_Y and a viscoplastic function g_{vp}. These functions will be defined in the next sections and are followed by a brief presentation of the numerical method implemented to solve the elasto-viscoplastic problem.

Governing equations The specific free energy $\boldsymbol{\psi}$ per unit volume is assumed to depend on two variables: the elastic left Cauchy-Green strain tensor $\mathbf{b}^{\mathrm{e}} = \mathbf{F}^{\mathrm{e}}\mathbf{F}^{\mathrm{e}\,T}$, and a scalar internal variable ξ that describes the isotropic hardening of the material. It is assumed that the material is isotropic and remains so during the process, which is admissible for moderated strains [17]. $\boldsymbol{\psi}$ is an isotropic function of $\mathbf{b}^{\mathrm{e}}$.

Utilizing data defined in the principal space, it is possible and convenient to use a reduced vector notation as introduced by Simo [18].

$$\boldsymbol{\beta} = \begin{Bmatrix} \beta_1 \\ \beta_2 \\ \beta_3 \end{Bmatrix}, \qquad \boldsymbol{\varepsilon}^{\mathrm{e}} = \begin{Bmatrix} \varepsilon_1^{\mathrm{e}} \\ \varepsilon_2^{\mathrm{e}} \\ \varepsilon_3^{\mathrm{e}} \end{Bmatrix}, \qquad \mathbf{1} = \begin{Bmatrix} 1 \\ 1 \\ 1 \end{Bmatrix} \tag{2}$$

The function that was chosen to model the free energy $\hat{\psi}$ and thus defines the constitutive behavior of the 316 stainless steel is displayed in equation 3.

$$\hat{\psi}(\boldsymbol{\varepsilon}_A^e, \xi) = \frac{1}{2}\lambda[\varepsilon_1^e + \varepsilon_2^e + \varepsilon_3^e]^2 + \mu[(\varepsilon_1^e)^2 + (\varepsilon_2^e)^2 + (\varepsilon_3^e)^2] + K(\xi) \tag{3}$$

The free energy is quadratic in the logarithmic principal elastic stretches, defined by $\varepsilon_A = \ln(\lambda_A)$, $A = 1, 2, 3$. In this function, elastic and plastic effects are uncoupled. The elastic part of $\hat{\psi}$ corresponds to a stretch based hyperelastic material. It is similar to the strain energy function used in small strain linear elasticity, except for the fact that logarithmic strain is used instead of the infinitesimal one [19]. Assuming such a free energy function provides the following stress/strain relationship:

$$\boldsymbol{\beta} = \mathbf{a}\boldsymbol{\varepsilon}^{\mathrm{e}}, \text{ where } \mathbf{a} = \lambda \mathbf{1} \otimes \mathbf{1} + 2\mu\mathbf{I}_3 \tag{4}$$

where λ and μ are the Lamé coefficients, $\boldsymbol{\beta}$ is the vector containing the eigenvalues of the Kirchhoff stress, $\boldsymbol{\varepsilon}^e$ is the vector of principal logarithmic elastic strains and $\mathbf{a}$ is the 3×3 matrix of elastic moduli in principal space. $\mathbf{I}_3$ is the 3×3 identity matrix and K is a function describing the isotropic hardening behavior of the material. The yield criterion f_Y was set to be the Von Mises criterion, classically used for metal [17]. It is given by equation 5, using principal stress.

$$f_Y(\boldsymbol{\beta}, \xi) = \|\mathrm{dev}(\boldsymbol{\beta})\| - \sqrt{\frac{2}{3}}[\sigma_Y + K'(\xi)] \tag{5}$$

The model thus obtained by assuming these forms of free energy function and yield criterion is the canonical J2-viscoplasticity, extensively discussed in the literature and classically used to represent the elasto-plastic and elasto-viscoplastic behaviors of metals (see for example [20] and [21]).

The next and last function to define to fully characterize the elasto-viscoplastic mechanical problem is the viscoplastic function g_{vp}. The widely used Norton's power law [20] was selected. It is defined by the following equation:

$$g_{\mathrm{vp}}(f_Y) = \frac{\sigma_Y}{\eta}(\frac{f_Y}{\sigma_Y})^m \tag{6}$$

where the exponent was set to $m = 1$, and η is a temperature-dependent "fluidity" coefficient, somewhat referring at the capacity that a solid has to behave like a fluid. To retrieve the rate-independent case, one has to set $\eta = 0$.

The numerical method chosen to deal with elasto-viscoplasticity was adapted from the one first introduced by Simo [18]. Its main component is a return-map algorithm in principal space. The algorithm, performed at each quadrature point of each element, is formed of the following steps:

1. Computation of the local total deformation gradient increment $\mathbf{dF} = \nabla(\Delta\mathbf{u}) + \mathbf{I}$

2. Removal of the shrinkage and thermal deformations from $\mathbf{dF}$

3. Computation of an elastic trial state

4. Computation of the eigenvalues of the trial strain tensor $\mathbf{b}^{\mathrm{e,tr}}$

5. Return mapping algorithm in principal space

6. Update of the intermediate configuration

This algorithm needs as input the local displacement increment vector $\Delta\mathbf{u}$ computed solving the global equilibrium of equation 14. Then, based on the internal variables at previous time step, the material state at the current one is computed. Details on the practical implementation of such an algorithm are available in [22] and [21]. However, features specific to the problem at hand had to be added. The original method considers a deformation gradient composed of two parts, $\mathbf{F}^{\mathrm{e}}$ and $\mathbf{F}^{\mathrm{p}}$. It can thus be applied directly in the current problem considering as deformed (spatial) configuration Ω_e instead of the actual one, namely Ω_{n+1} (see figure 2). Some manipulations were thus necessary to not only compute the elasto-viscoplastic effects using Simo's method with the appropriate input deformation gradient, but also to retrieve the output data expressed in the actual reference configuration in order to solve the equilibrium of equation 14.

 These additional steps are the following:

1. Removal of the thermal and shrinkage deformations
   In order to properly use Simo's algorithm, it is necessary to use a deformation gradient increment that does not include the deformations due to shrinkage and dilatation. Similarly to the decomposition of the total deformation gradient of equation 1, the deformation gradient increment can be expressed as: $\mathbf{dF} = \mathbf{dF}^{\mathrm{e}}\mathbf{dF}^{\mathrm{p}}\mathbf{dF}^{\theta}\mathbf{dF}^{\mathrm{s}}$. From this formula, an elasto-viscoplastic deformation gradient increment can be retrieved. It is the one that is used to compute the elastic trial state and that enters the return map algorithm.

$$\mathbf{dF}^{\mathrm{ep}} = \mathbf{dF}^{\mathrm{e}}\mathbf{dF}^{\mathrm{p}} = \mathbf{dF}^{\theta\,-1}\mathbf{dF}^{\mathrm{s}\,-1}\mathbf{dF} \tag{7}$$

2. Push forward of the local tangent and Kirchhoff stress tensor to the spatial configuration
   The local tangent $\mathbf{c}$ and Kirchhoff stress tensor $\boldsymbol{\tau}$, that are the outputs of the viscoplastic algorithm, are computed in the elastic configuration Ω_e of the figure 2. It is necessary to transport them to the appropriate configuration using adequate pull-back and push-forward operations (see for example [23]). The global equilibrium equation (see eq. 14) includes the global tangent $\mathbb{C}$ and 2nd Piola-Kirchhoff stress tensor $\mathbf{S}$, that are assembled using integration point data returned by the local elasto-plasticity algorithm. They are both material tensor i.e. they are expressed in the initial configuration Ω_0. To transport $\mathbf{c}$ to this configuration, a pull-back transformation is made using the deformation gradient tensor $\mathbf{F}^{\mathrm{ep}} = \mathbf{F}^{\theta\,-1}\mathbf{F}^{\mathrm{s}\,-1}\mathbf{F}$. To assemble $\mathbf{S}$, the Kirchhoff stress tensor returned by the viscoplastic algorithm, which is a spatial tensor, is first pushed-forward to the current configuration Ω_{n+1} using the deformation gradient $\mathbf{F}^{\theta\mathrm{s}} = \mathbf{F}^{\theta}\mathbf{F}^{\mathrm{s}}$. Then, using proper relationships, the 2nd Piola-Kirchhoff stress tensor is retrieved from the Kirchhoff stress tensor. All the calculations related to those transformations are regrouped equation 8.

$$\mathbb{C}^{IP}_{IJKL} = F^{-1}_{Ii}F^{-1}_{Jj}\mathbf{c}_{ijkl}F^{-1}_{Kk}F^{-1}_{Ll} \tag{8}$$

$$\boldsymbol{\tau}_{\Omega_{n+1}} = \mathbf{F}^{\theta\mathrm{s}}\boldsymbol{\tau}\mathbf{F}^{\theta\mathrm{s}\,T}$$

$$\mathbf{S}^{IP} = \mathbf{F}^{-1}\boldsymbol{\tau}_{\Omega_{n+1}}\mathbf{F}^{-T}$$

The superscript $[\bullet]^{IP}$ precises that the variable is considered at integration point level, where an ambiguity is present.

2.2.3 Thermal deformations

The thermal strains are introduced through a deformation gradient $\mathbf{F}_\theta$. Since isotropy is assumed, $\mathbf{F}_\theta$ is a spherical tensor[1]. As proposed by Vujosevic [24] the formula of equation 9 was used to calculate the deformation gradient tensor variation due to the temperature evolution between times t_n and t_{n+1}.

$$\mathbf{dF}_\theta = \int_{T_n}^{T^{n+1}} \vartheta(T)dT\ \mathbf{I} \tag{9}$$

where $\vartheta(T)$ is the temperature dependent thermal expansion coefficient.

2.2.4 Shrinkage deformations

The shrinkage deformations are computed using the powder fraction variable ψ returned by the thermal model phase change algorithm. As for the thermal deformations, isotropy is assumed which lead to a spherical tensor computed as in equation 10. This formula describes the deformation gradient tensor variation relative to the volume reduction due to the transformation from powder of porosity ϕ to consolidated material between times t_n and t_{n+1}.

$$\mathbf{dF_s} = \varphi(\boldsymbol{\psi})\mathbf{I} \text{ where : } \varphi(\boldsymbol{\psi}) = \left(\frac{1 - \boldsymbol{\psi}_n\phi}{1 - \boldsymbol{\psi}_{n+1}\phi}\right)^{1/3} \tag{10}$$

2.3 Mechanical properties

To fully characterize the elastic behavior of the 316L stainless steel, two parameters are needed. Here the Poisson ratio and the Young modulus were chosen. The Poisson ratio ν was kept at a constant value of 0.29. The Young modulus E (GPa) is temperature-dependent according to formulas obtained with interpolations and extrapolations based on experimental data from [25].

$$E(T) = \begin{cases} 205, & \text{for } T \leq 830 \text{ K} \\ 205.91 - 2.6913e{-}2(T + 273.15)- & \\ 4.1876e^{-5}(T + 273.15)^2, & \text{for } T \leq 1125 \text{ K} \\ -0.0169 \times T + 27.89, & \text{for } T \leq T_{\text{sol}} \\ 2e-2, & \text{for } T > T_{\text{sol}} \end{cases} \tag{11}$$

The yield stress σ_Y and the thermal expansion coefficient are considered temperature dependent as well. Their thermal evolutions were inter- and extrapolated from experimental data retrieved from [25].

The hardening behavior of the 316 stainless steel was assumed to be isotropic only. The main motive for which the kinematic hardening was not represented is that the Bauschinger effect is not preponderant, which legitimates the use of an isotropic hardening function [26]. The isotropic hardening function K was defined as a Voce-type function [27], given by equation 12.

$$K(\xi) = (\sigma_s - \sigma_1)(1 - \exp(n_v\xi)) \tag{12}$$

It can be interpreted as the evolution of the yield stress from an initial value σ_1 to a saturation value σ_s. The constant n_v determines the rate at which the initial stress tends to the saturation value. This function was proved to best represent the hardening behavior of the 316L stainless steel, especially at elevated temperatures, as shown by Singh [28]. The functions describing the temperature-dependence of the three parameters σ_s, σ_1 and n_v were obtained from inter and extrapolation of the data reported in this article. The values that were used are the ones determined for the smallest grain size available (i.e. 2.7 µm). Indeed, considering the very high ($> 10^5$ K s^{-1} [29, 30]) cooling rates to which the material is exposed during its SLM-processing, the grain sizes are in the order of magnitude of few microns or less [31].

---

[1] $\mathbf{A} = k\,\mathbf{I}, k \in \mathbb{R}$

2.3.1 Fluidity coefficient

The fluidity coefficient η ($Pa^{-1} s^{-1}$) in solid phase at high temperature is comparable to a viscosity, i.e. it represents the ability that a solid has to behave like a fluid. It was modeled with a temperature dependent function. Data on this parameter, especially in the solid phase temperature range, is scarce. A model was assumed, based on the Lemaitre recommendation [15] which states that viscous effects appears at roughly one-third of the melting temperature. Consequently, a null viscosity was set for $T \leq \frac{T_{\mathrm{sol}}}{3}$, and the liquid steel viscosity, retrieved from [32], was used when $T = T_{\mathrm{sol}}$, i.e $6.7.10^{-3}$ $Pa^{-1} s^{-1}$. A linear interpolation was then made between these two temperatures.

2.3.2 Treatment of the liquid/mushy zone and the powder

The material that is modeled is present under three phases: bulk, liquid and powder. The bulk material behavior does not apply for the two other phases, for which specific constitutive equations had to be implemented. The method that was adopted is the one proposed by Koric & Thomas [33] for molten metal modeling in casting simulations. The objective is to derive a constitutive behavior that imposes negligible stress in these phases without introducing a different treatment of the liquid/powder elements in the finite element assembling, which would be cumbersome from a technical point of view. Among the two techniques suggested in this reference, the so-called "elastic-perfectly plastic model" was selected. It consists in setting for elements with $T \geq T_{\mathrm{sol}}$ or $y_{\mathrm{pow}} > 0$ a low yield stress (typically $0.02\,\mathrm{MPa}$), to enforce small stress values without giving birth to numerical issues, with no hardening, and then use the regular radial-return algorithm.

2.4 Model formulation

The equation which governs the mechanical behavior of the part is the linear momentum equilibrium. Although the transient thermal field induces dynamic variations of stress and strain around the laser beam heated area, the global domain remains static during the process. Consequently, the problem was considered as quasi-static (similarly to [34, 12, 35] for example).
This translates into the following strong formulation:

$$\begin{cases} \nabla \cdot \mathbf{P} + \mathbf{b_0} &= 0 & \text{in } \Omega_0 \\ \mathbf{u} &= \overline{\mathbf{u}} & \text{on } \Gamma_D \\ \mathbf{T} &= \overline{\mathbf{T}} & \text{on } \Gamma_N \end{cases} \tag{13}$$

Where the first line corresponds to the static linear momentum equilibrium expressed in terms of the first Piola-Kirchhoff stress $\mathbf{P}$ and where $\mathbf{b_0}$ is the body forces density inside the part (here, gravity forces only) and $\mathbf{u}$. The two subsequent lines correspond to the boundary conditions, where $\overline{\mathbf{u}}$ is a prescribed displacement and $\overline{\mathbf{T}}$ is a prescribed force. In the present problem there are neither imposed displacement nor force, so $\overline{\mathbf{T}} = 0$ and $\overline{\mathbf{u}} = 0$. An illustration of the domain and the surface corresponding to Γ_D and Γ_N can be found in figure 3.

For later use, the 2nd Kirchhoff stress tensor $\mathbf{S} = \mathbf{F^{-1}} \cdot \mathbf{P}$ is introduced.

The approach chosen to derive the linearized weak formulation is the so-called Updated Lagrange (UL) formulation. Its main characteristic is to take as reference configuration the last converged one, Ω_n, instead of the initial Ω_0 [36]. The main advantage of this method for the present problem is the possibility to compute the thermal problem on the "real" geometry. Indeed, the mesh is updated at the end of every time step so the thermal transfers are computed on the last converged configuration. Since the deformation map φ includes the volume reduction resulting from the transformation from powder to consolidated material, the issue of "mass creation" introduced earlier is addressed leaving untouched the thermal problem formulation and implementation. This is of great interest from a practical point of view with respect to a Total Lagrange (TL) formulation. The linearized UL formulation of the problem to be solved finally reads: (technical
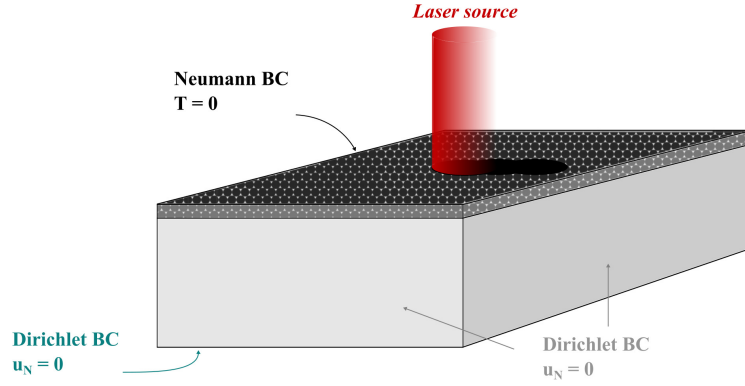
Figure 3: Model and mechanical boundary conditions.
u_N stands for the displacement component normal to the surface

details on the calculations are available in Leger et al. [37])

$$\int_{\Omega_n} \tilde{\mathbf{S}} : (\nabla_{X_n}^T (\Delta \varphi) \cdot \nabla_{X_n} (\delta \varphi)) dV_n +$$

$$\int_{\Omega_n} \tilde{\mathbb{C}} : (\mathbf{F_{n \to n+1}}^T \cdot \nabla_{X_n}^T (\Delta \varphi)) :$$

$$(\mathbf{F_{n \to n+1}}^T \cdot \nabla_{X_n}^T (\delta \varphi)) dV_n =$$

$$\int_{\Omega_n} \mathbf{b_n} \cdot \delta \varphi \, dV_n - \int_{\Omega_n} \tilde{\mathbf{S}} : (\mathbf{F_{n \to n+1}}^T \cdot \nabla_{X_n}^T (\delta \varphi)) dV_n$$

(14)

With:

$$\mathbf{b_n} = \frac{1}{\det(\mathbf{F}_{0 \to n})} \mathbf{b_0}$$

$$\tilde{\mathbb{C}}_{mnop} =$$

$$\frac{1}{\det(\mathbf{F}_{0 \to n})} \mathbb{C}_{ijkl} (\mathbf{F}_{0 \to n})_{mi} (\mathbf{F}_{0 \to n})_{nj} (\mathbf{F}_{0 \to n})_{ok} (\mathbf{F}_{0 \to n})_{pl}$$

$$\tilde{\mathbf{S}} = \frac{1}{\det(\mathbf{F}_{0 \to n})} \mathbf{F}_{0 \to n} \cdot \mathbf{S} \cdot \mathbf{F}_{0 \to n}^T$$

The last two relationships correspond respectively to the push-forward of the tangent and the Second Piola-Kirchhoff stress from the initial configuration Ω_0 to the reference configuration Ω_n, illustrated in figure 2.
$\delta \varphi$ is a test function, while $\Delta \varphi$ is the unknown deformation map variation to be computed.

3 Numerical validation & consistency check of the model

3.1 Numerical validation

The mechanical solver was confronted with numerical results from the literature. For that purpose, the uniaxial tension test of Auricchio & Taylor [38] was reproduced to verify the correct implementation of the mechanical solver and the material constitutive behavior. It consists in a single cubic element loaded controlling the displacements. The two models were compared in term of stress/strain response. The results are displayed in figure 4.

3.2 Physical consistency of the model

To partially address the lack of experimental validation of the mechanical model, its physical consistency was checked in order to qualitatively verify its ability to represent the SLM process millimeter-scale thermo-mechanical phenomena. Generally speaking, thermal stresses appear when a volume cannot expand or shrink without impediment after a local temperature modification.
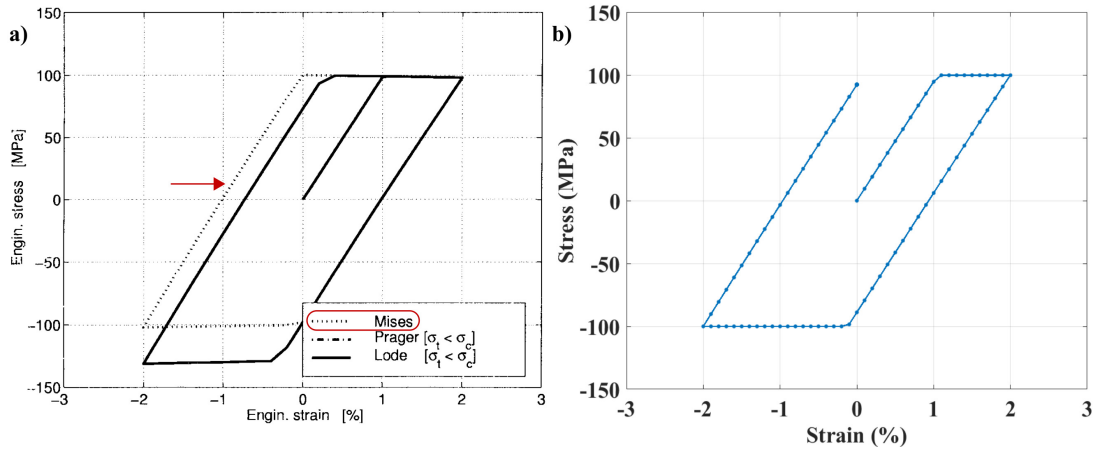
Figure 4: Numerical validation computational experiment results. a) Results from Auricchio & Taylor b) Our results

More specifically, two phenomena were identified in the literature (see for example [39, 40] or [41]) as creating the residual stresses observed in the SLM-built parts:

- *The Thermal Gradient Mechanism (TGM)*: The thermal expansion of the laser heated material is hindered by the surrounding colder material which results in compressive stress in the heat affected zone. Since the yield stress at high temperature is low, plastic strain appears to limit the stress to admissible levels. When the laser moves away from the area, the material cools down and shrinks. During this stage, tensile stress appears in the plastically deformed area.

- *The cool down*: At the end of its processing, the top layer is at a higher temperature than either the substrate or the previously built layers. Consequently, its contraction is larger than in the underneath material. This contraction is thus restrained, which gives birth to tensile stress in the top layer and compressive stress in the underlying ones.

Figure 5 shows a section of the part during the processing of the first track along a xz plane. The areas of tension-compression characteristic of the TGM described earlier are clearly visible and in accordance with the temperature and plastic strain fields. Indeed, the accumulated plastic strain ξ, that has non-zero values only where plastic deformation occurs, is significantly high close to the surface, where the model predicts the appearance of tensile stress.

Figure 6 shows the same section at the end of the simulation. The superficial area of tensile stress and the underneath area of compression typical of the cool down mechanism are distinctly observable.

Finally, as experimentally evidenced by Simson et al [41], the through-thickness evolution of the stress in the final state features an initial increase on a reduced height, followed by a monotonous decrease. This behavior was reproduced by the model as illustrated in figure 7. This figure shows as well that the stress in the building direction is significantly smaller than in the x and y directions. This is in accordance with the fact that the upper surface has a free BC that allows the part to expand freely in the z direction. All the preceding observations confirm that the simulation was able to reproduce the main empirically evidenced phenomena that give birth to residual stress and plastic strain. In absence of a full experimental validation, it nonetheless ensures the qualitative correct thermo-mechanical behavior of the model.
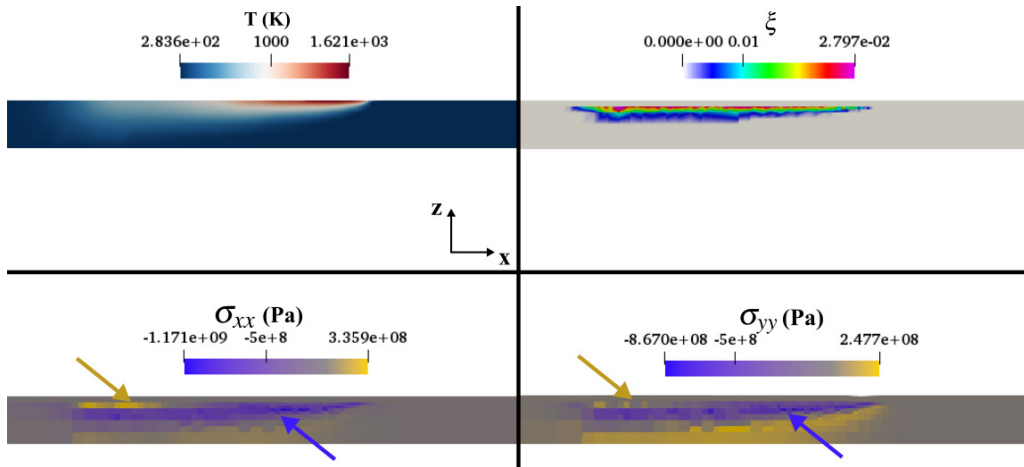
Figure 5: Thermal gradient mechanism. The blue arrows indicates the area in compression in the heat affected zone. Yellow arrows indicate the area in tension after the laser moved away.
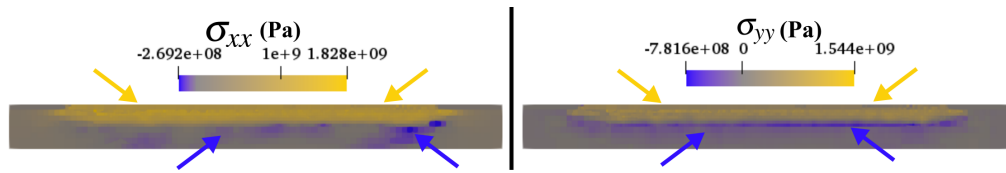

Figure 6: Cool down residual stresses. The blue arrows indicates the area in compression that restrain the top surface contraction. Yellow arrows point out the superficial area in tension.
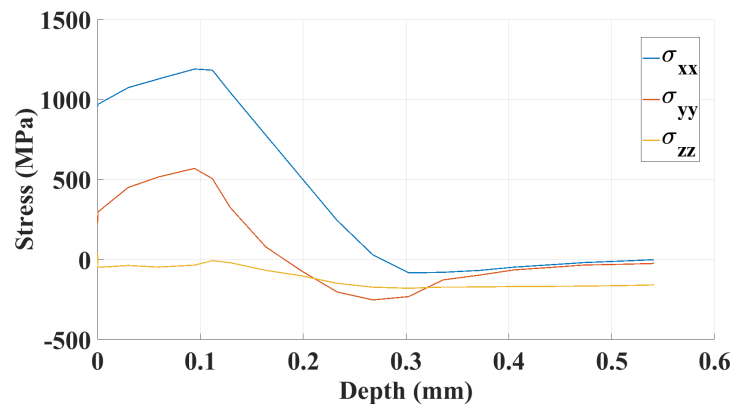

Figure 7: In depth stress tensor diagonal component evolutions

4 Analyses of residual stress, plastic strain and geometrical error formation mechanisms

4.1 Computational experiments

The computational experiment that was run is illustrated in figure 8. It is a millimeter-scale, three-track and single-layer simulation. A 2x2 full factorial design of experiment with a central point was performed, the variable parameters being the laser speed and power. The corresponding sets of variable parameters are regrouped table 1. The main fixed parameters in the computational experiments are listed table 2. The processing time amounts to 28 ms and extra 100 ms of cooling time were simulated. The time discretization was performed using a classic backward Euler scheme. The time step size was set to 4.10^{-5}s. The space discretization was done using standard Lagrange linear elements. At the beginning of the simulation, the total number of element amounted to 26400 and fluctuated subsequently according to a mesh refinement algorithm. The model was implemented using the open source finite element library deal.ii [42] (more details on the technical aspects can be found in a previous article [14]). The simulations lasted approximately 8 hours each on a desktop computer (4 cores (8 threads) at 3.6GHz with 24 Go of memory). The Newton iterations were deemed to have converged when the normalized residual norm (norm of the residual divided by the norm of the residual at the first iteration) was smaller than 10^{-5}.
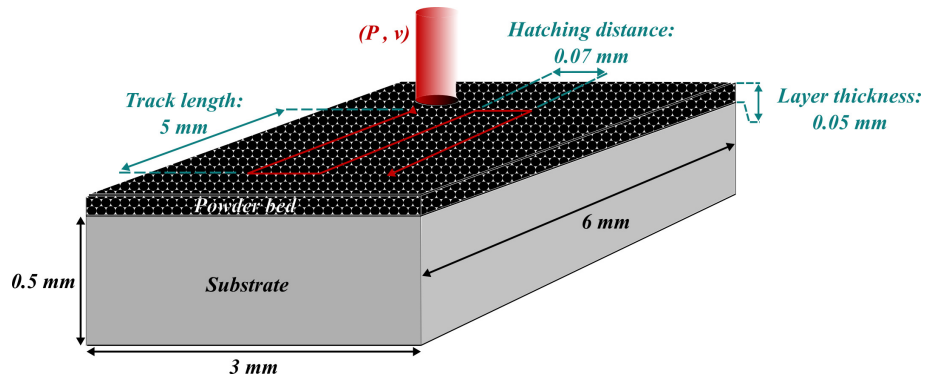

Figure 8: Computational experiment scheme

The outputs of the simulation that will be studied are the widths and lengths of the three melted tracks, the Von Mises stress and the accumulated plastic strain values in the processed material.

Table 1: Preliminary design of experiment for the mechanical solver validation

Set #	Laser Speed (mm/s)	Laser Power (W)	Energy density ($\mathrm{J\,mm^{-3}}$)
0	500	100	57
1	500	200	114
2	350	150	122
3	200	100	143
4	200	200	285

Preliminary thermal-only simulations showed that the couple (100,500) is outside the processing window and will not be considered in the thermo-mechanical analysis.
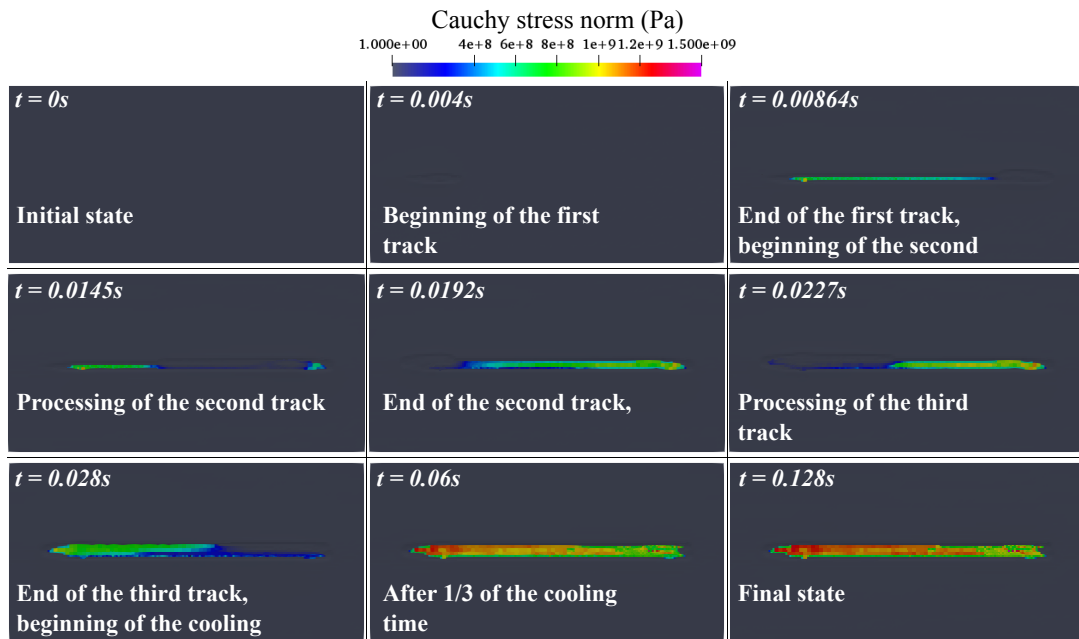
Cauchy stress norm (Pa)
1.000e+00   4e+8 6e+8 8e+8 1e+91.2e+9 1.500e+09

t = 0s **Initial state**	*t = 0.004s* **Beginning of the first track**	*t = 0.00864s* **End of the first track, beginning of the second**
t = 0.0145s **Processing of the second track**	*t = 0.0192s* **End of the second track,**	*t = 0.0227s* **Processing of the third track**
t = 0.028s **End of the third track, beginning of the cooling**	*t = 0.06s* **After 1/3 of the cooling time**	*t = 0.128s* **Final state**

Figure 9: Cauchy stress evolution during the material processing and cooling time - Parameter set #1

ξ
0.000e+00   0.02   0.04   0.06   9.000e-02

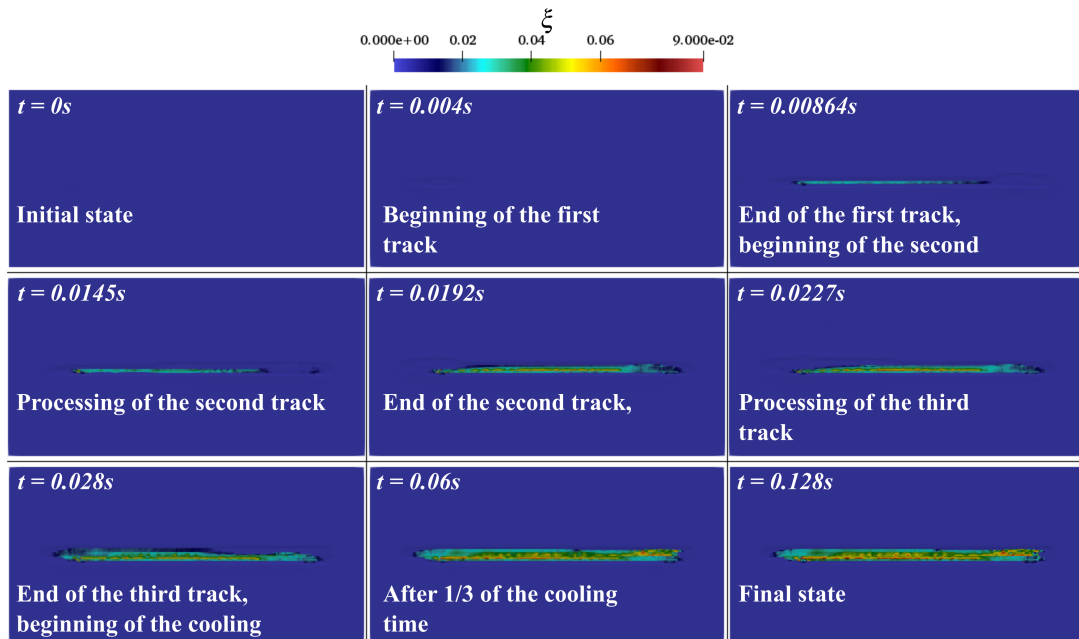|		
t = 0s **Initial state**	*t = 0.004s* **Beginning of the first track**	*t = 0.00864s* **End of the first track, beginning of the second**
t = 0.0145s **Processing of the second track**	*t = 0.0192s* **End of the second track,**	*t = 0.0227s* **Processing of the third track**
t = 0.028s **End of the third track, beginning of the cooling**	*t = 0.06s* **After 1/3 of the cooling time**	*t = 0.128s* **Final state**

Figure 10: Plastic strain evolution during the material processing and cooling time - Parameter set #1

Table 2: Simulation campaign fixed parameters

| Parameter	Value
Material	AISI316L stainless steel
Powder granulometry	30 μm
Hatching distance	70 μm
Layer thickness	50 μm
Convection coefficient	20 W m^{-2} K^{-1}
Ambient temperature	298 K
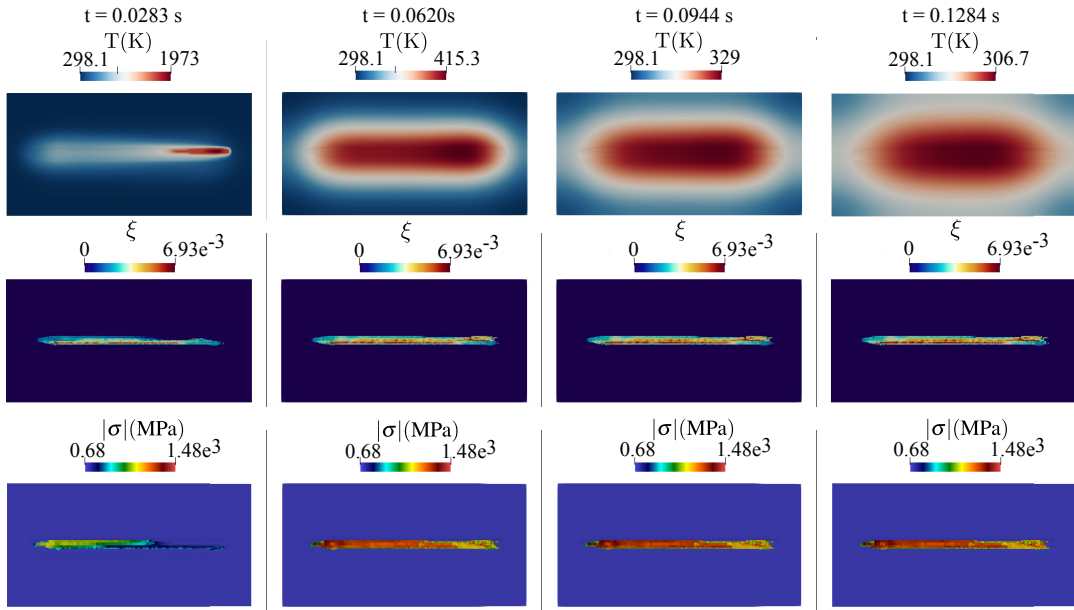
Figure 11: Temperature, Cauchy stress and plastic strain evolutions during the cooling phase - Parameter set #1

4.2   Analyses of residual stress & plastic strain formations

The particularly high levels of stress in the final state are in accordance with previous works, both experimental [6] and numerical [43, 44]. Indeed the elevated cooling rates give birth to high thermal strains and as a consequence high stresses. These mechanisms explain as well the position of the local maxima. They are positioned at the beginning and the end of each track. It corresponds to the peak temperatures as well as the highest heating/cooling rate locations, due to the laser ignitions and extinctions. This phenomenon was observed experimentally by Zhang et al. [45]. However the maximal values visible in figure 9 (1.5×10^3 MPa) may appear as disproportionate in regard of the ultimate tensile stress of the AISI316L stainless steel, i.e. 500MPa at room temperature [46]. This is most probably due to the Voce's parameters temperature dependence. The functions that were implemented are inter- and extrapolation from data retrieved from the literature, and may thus contain imprecisions, especially at high temperatures where the empirical information is scarce. It is probable that overestimation of the hardening saturation stress σ_s at high temperature led to excessive yield stress values and as a consequence to oversize Von Mises stress. This highlights the utility of a thorough experimental calibration procedure to feed the model with accurate and reliable input data. As displayed in figure 13, local peaks of plastic strains are located as well at the track extremities. Similarly to the residual stress, it can be
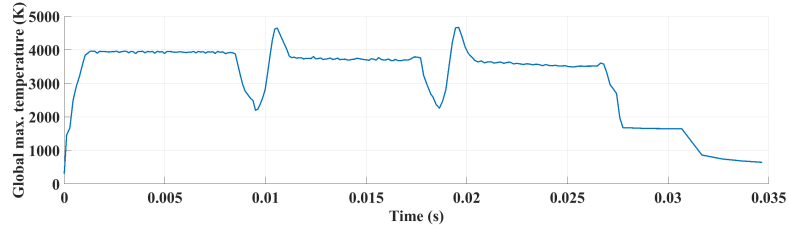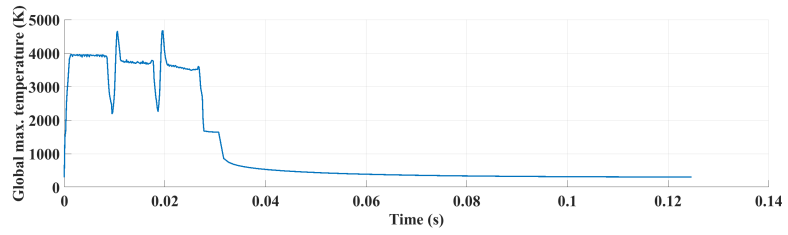
(a) Global maximal temperatures time evolution - Parameter set #1
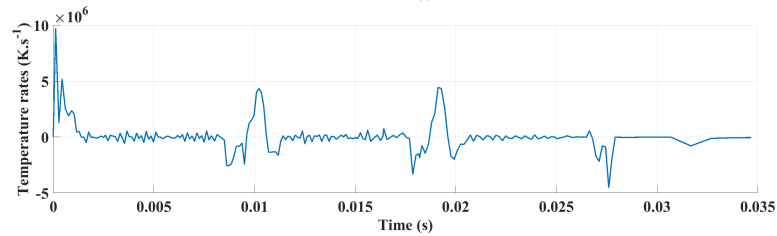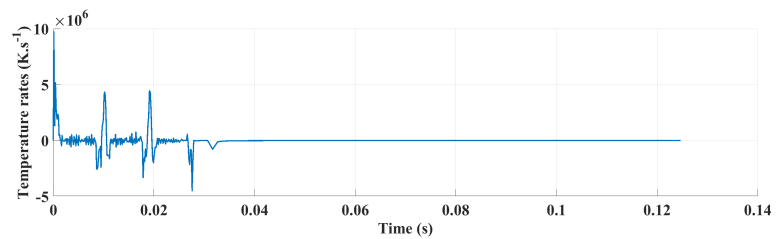
(b) Temperature rates time evolution - Parameter set #1

Figure 12: Global maximal temperatures and temperature rate time evolution.
Top: Full simulation.
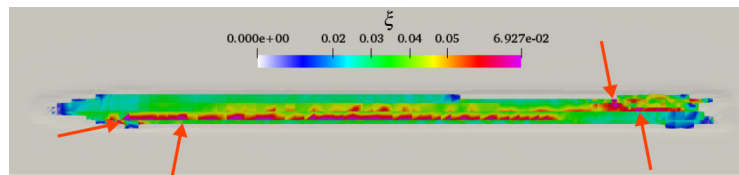Bottom: Magnification of the processing time.

Figure 13: Final plastic strain field. Orange arrows indicate the strain peak value points - Parameter set #1

explained by the fact that the heating/cooling rates are the highest in these areas. More globally, figure 10 discloses that the plastic strains tend to decrease with the number of processed track, i.e. $\xi_{track1} > \xi_{track2} > \xi_{track3}$. This is in accordance with the maximal temperature and temperature rates time evolutions, illustrated in figure 12a and 12b. In fact, the time dependence of the global temperature maximum is enlightening to explain the final stress and plastic strain fields. First, it can be seen on this graph that the maximal temperature in the steady state of one track tends to diminish when the number of track increases. Then, it shows peak values of both temperature and temperature rates at the times corresponding to the first instants of each track processing. Their localizations are at the beginning of the tracks, i.e. where the laser beam is being switched on and the heating rates are the highest, as shown in figure 12b. These observations underline the relationship between peak temperatures, cooling rates and plastic strain formation. This makes it possible to use thermal data to anticipate the most critical areas in term of distortion defects, which is of importance during the process design stage. It also highlights the importance of temperature field control in the quality of the parts produced by SLM.

Figure 11 presents more specifically the time evolution during the cooling phase of the temperature, stress and plastic strain. It can be seen that the major part of the residual stress develops during the first instants after the end of the processing phase, i.e. right after the laser is being switched off. This is consistent with the fact that it corresponds with the period in which cooling rates are the highest, and in which the material is getting stiffer, due to the thermal dependence of the 316L stainless steel mechanical properties. Indeed, the global temperature decrease rapidly since no heat input is provided to the part anymore. Figure 11 also discloses an increase in the plastic strain values at constant stress (between t=0.0944 s and t=0.1284 s). While most of the thermal stress develops in the first milliseconds after the heat source is being switched off, the plastic strains continue to grow up until the end of the simulation. These deformations at constant stress in the area where the material is at a high temperature reflects the viscoplastic behavior implemented.

Strategies to lower the residual stresses were already proposed in the literature. One of the most popular and easy to implement is substrate preheating [47, 45]. In has two effects in reducing the stress: it diminishes the thermal gradients by increasing the material minimum temperature and lowering the rigidity of the substrate since the Young modulus is reduced when the material is heated.

All the previous observations lead to a conclusion similar to the one that was drawn by Bruna-Rosso et al. [14] for the reduction of lack of fusion porosities, i.e. in-process variable parameters would be beneficial to improve the quality of the part produced. While the lack of fusion defects reduction suggested to modify the scanning strategy between the first tracks, the plastic strain and residual stress creation mechanisms put forward the utility of varying the process parameters within the track itself. In fact considering a gradual laser power at the beginning and the end of each track, i.e. a progressive switch on/switch off of the laser beam appeared as relevant in order to reduce the heating/cooling rates. It would compensate the acceleration/deceleration of the beam when a track starts or ends to keep the energy density constant. Empirical studies are investigating this topic [48]. However, considering the current industrial hardware capacities, scanning strategies with variable parameters cannot be implemented on commercial machines, and are thus for now confined to the research field.

Then, the results of the four simulations of the parametric analysis were compared and analyzed in terms of maximal and mean global Von Mises stress and residual strain at the last computed time step. Their values for the four sets of parameters simulated are given in tables 3 and 4.

Table 3: Global thermo-mechanical simulations Von Mises stress mean values and maximal values

Speed (mm/s)	Power (W)	Energy density ($\mathrm{J\,mm^{-3}}$)	Max. stress (MPa)	Mean stress (MPa)
500	200	114	923	1.15×10^3
350	150	122	899	1.13×10^3
200	100	143	865	1.12×10^3
200	200	285	978	1.45×10^3

As discussed in the previous section, the values of the Von Mises stress are excessive with respect to the AISI stainless steel mechanical properties. Moreover, the lack of experimental validation

Table 4: Global thermo-mechanical simulations plastic strain mean values and maximal values

Laser speed (mm/s)	Laser power (W)	Energy density ($\mathrm{J\,mm^{-3}}$)	Max. strain	Mean strain
500	200	114	0.030	0.35
350	150	122	0.029	0.18
200	100	143	0.028	0.082
200	200	285	0.051	0.23

prevents to consider the absolute values of the simulation outputs as fully reliable. However, the model behavior is consistent with experimental observations. That is why it was deemed relevant to investigate relative levels and tendency with respect to input parameters modifications.
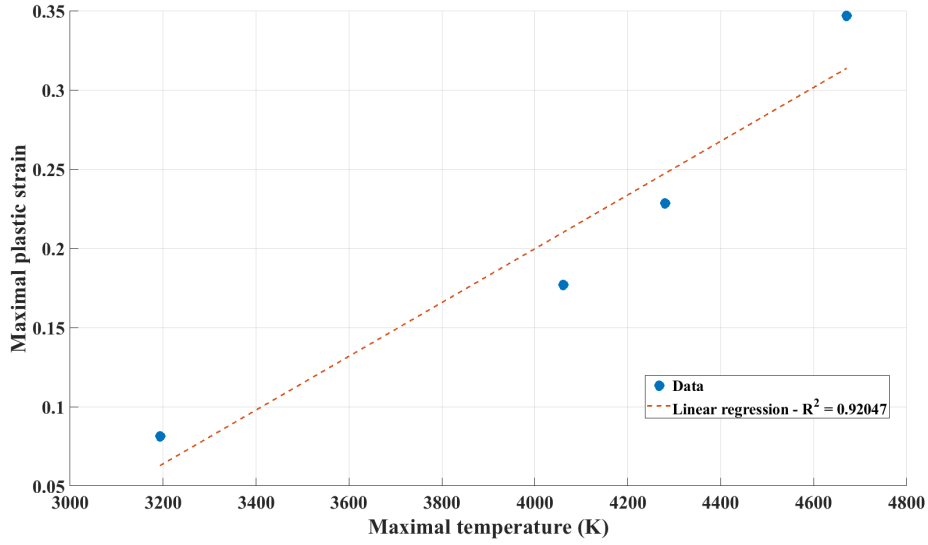

Figure 14: Linear regression $\xi_{\mathrm{max}} = f(T_{\mathrm{max}})$

A close relationship between plastic strain and maximal temperature is disclosed when plotting the curve $\xi_{\mathrm{max}} = f(T_{\mathrm{max}})$, as displayed in figure 14. The linear regression has a good coefficient of determination R^2 which supports the affine correlation between the maximal plastic strain and the maximal temperature. It can be explained by the fact that high peak temperatures give birth locally to elevated thermal gradients and cooling rates which then engender thermal deformations and stress beyond the metal elastic limit. Table 4 shows that locally the plastic strains can exceed 20%. As a consequence, one should keep in mind to adjust the process parameters and the experimental setup to moderate peak temperatures, such as an efficient gas flow when the laser is working.

The mean of the Von Mises stress $\bar{\sigma}_{\mathrm{VM}}$ seems to depend linearly on the laser power, but has a more complicated behavior with respect to the laser velocity. Indeed when observing the curve of figure 15 a correlation can be found between $\bar{\sigma}_{\mathrm{VM}}$ and the fraction $\frac{P}{v^2}$ with an excellent coefficient of determination. This result is interesting from a process design point of view. Indeed, for now, one of the main variables taken into account to determine whether a set of parameter was suitable or not is the volumetric energy density. It was proven to be efficient in determining the region where the heat input in high enough to melt the required amount of powder. However, Scipioni Bertoli et al. [49] demonstrated that this factor alone is not sufficient to determine the feasibility window. Other criteria should be considered to further restrain this window to avoid the appearance of other detrimental phenomena such as the keyhole effect. For instance, King et al. [50] proposed the normalized enthalpy ≤ 6 to determine adapted process parameters to remain in conduction mode. The result correlating σ_{VM} to the fraction $\frac{P}{v^2}$ suggests that an additional criteria could be considered to avoid excessive residual stress, and consequently excessive thermal distortions.
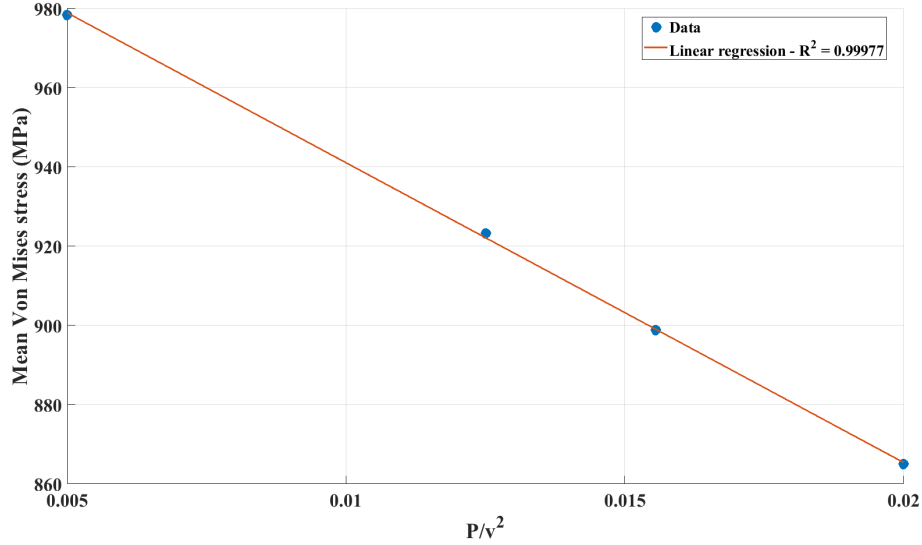
Figure 15: Linear regression $\overline{\sigma}_{\mathrm{VM}} = f(\frac{P}{v^2})$

This criterion would be directly related to $\frac{P}{v^2}$. However, a deeper and broader investigation to determine a more reliable and widely valid relationship $\sigma_{\mathrm{VM}} = f(\frac{P}{v^2})$ is necessary, since only four sets of parameters were tested to obtain the regression of figure 15.

4.2.1 Final geometry analyses

Performing thermo-mechanical simulations demonstrated that the local geometry does not depend on mechanical phenomena but rather on thermal ones, i.e. on the molten pool dimensions. Table 5 regroups the final dimensions of the three tracks together for the four sets of parameters simulated. The parametric analysis showed that the width is strongly related to the process parameters, and more specifically to the energy input density. Indeed, simulation 3 shows an increase in the width of 80 microns with respect to the others. It corresponds to an excess of 230 microns with respect to the nominal width (140 microns) while the other simulations showed an excess of 150 microns. This phenomena was shown experimentally by Demir and Previtali [10]. The authors report errors of 50 to 250 µm depending on the process parameters and scanning strategy, which is in the same order of magnitude than the numerical results. Here appears the influence of the melt pool size on the final local dimensional properties of the part. Indeed, increased dimensions of the molten pool result in oversize consolidated material area, as illustrated in figure 16. However the rather coarse spatial discretization did not allow to discriminate the set of parameters with similar energy density.

The length appeared less sensitive to the process parameters. It can be explained as follow. First, the heat source depends on the laser speed through its geometric parameters as described in Bruna-Rosso et al. [14]. The extra length depends on the size of the melt pool solely at the beginning and the end of each track, unlike the width that is influenced by its dimensions all along the track. Second, the laser speed is position dependent, i.e. it accelerates at the beginning of each track and decelerates at the end at a constant rate. Consequently, in the first instants of each track processing, the speed is the same for all the set of parameters, which explains the similar melt pool dimensions it these areas and the following similar lengths. However the error between nominal (5 mm) and measured length (5.5-5.6 mm) is significant. This is most probably due to an overestimation of the length by the simulations. In fact, the Goldak heat input model was developed and experimentally calibrated in permanent regime. As a results, it provides reliable quantitative results in permanent regime, i.e. when the melt pool reaches a stable size, as demonstrated by Bruna-Rosso et al. [14]. However, at the beginning and end of the tracks the transient regime is less well represented by the heat input model that is implemented. These results suggest to better describe the laser source in

these regions to obtain more accurate track length estimations.

Table 5: Final melted area widths and lengths

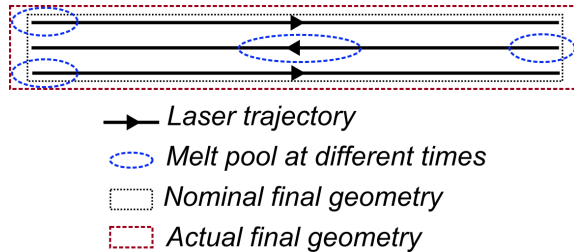| Energy density ($\mathrm{J\,mm^{-3}}$)	Length (mm)	Width (mm)
114	5.6	0.29
122	5.6	0.29
143	5.5	0.29
285	5.6	0.37

Figure 16: Mechanism of oversize dimensions due to the melt-pool

The results showed as well the importance of taking into account the extra thickness of molten material brought by the melt pool dimensions in the part and process design to avoid the geometrical errors beforehand, i.e. at design stage. Indeed, the discrepancy induced by this phenomenon amounts from few dozen to few hundreds µm. If this is acceptable for many applications where the dimensions of the parts are few dozen mm or more, or where a post-processing stage can correct it, this difference between designed and actual geometry can be very detrimental for applications such as cardiovascular stents [10] due to their geometrical specificities. Indeed, their minute dimensions, with strut widths as small as few hundreds microns, render the error proportionally significant. Moreover their intricate geometries make post-process corrections challenging while their functionality strongly depends on their size [11]. The model can provide an estimation of the downsizing of the theoretical geometry to perform in order to compensate the extra molten material. The computational experiment spatial discretization is rather coarse with respect to the geometry of the molten metal area. This brings significant uncertainty and error to the dimension measurements. However simulations with a finer mesh can be planned to have a better quantification of the effect of the melt-pool dimensions on the geometrical errors. Besides, a wider range of parameters could be tested and an adapted computational DoE could be perform. A simple empirical model can be derived linking the process parameters (P,v) and the scaling to apply to the nominal dimensions in order to obtain a final geometry closer to the nominal one. Moreover, if a more localized and precise correction is to be planned due to the space variations of the melt pool dimensions, the model can provide quantitative information on the local process parameters modifications to make to compensate them.

5   Conclusion

An original finite strain mechanical solver was developed for stress, plastic strain and final geometry computation at millimeter scale during the selective laser melting of AISI316L stainless steel powder. It takes as input the temperature and powder fraction fields calculated using a previously developed thermal model. The residual stresses, plastic strains and distortions resulting from the material temperature variations and phase transformations were computed in order to better understand and predict the geometrical errors. This thermo-elasto-viscoplastic FEM was first numerically validated since it was able to replicate data retrieved from the literature. Its ability to represent the in-process thermo-mechanical behavior of the manufactured material was

then qualitatively checked. Comparisons of the computed data with empirical results from the literature showed the ability of the model to reproduce two major phenomena, namely thermal gradients and cooling down. Finally, a computational design of experiment was run to get insight into the formation mechanisms of plastic strain and residual stress and the effects of two of the main SLM process parameters, namely powder P and laser speed v. Their effects on the final geometry of the final melted area dimensions were scrutinized. The results obtained from these simulations led to the main following conclusions:

- Areas that are the most at risk of cracking due to excessive stress are located close to the lateral surfaces of the built part

- The peak plastic strain values, reflecting the risk of cracking, are correlated to the maximal temperatures

- Local geometrical errors are related to thermal phenomena only (excessive/too small melt pool dimensions)

- The heat input model should be modified in the transient regime to have more accurate estimations of the track lengths

- Global geometrical errors (distortions), consequence of residual stresses, can be tuned through the fraction $\frac{P}{v^2}$

- Local variation of the heat input volumetric density due to the laser speed variations should be compensated by a varying power

- Excessive heating/cooling rates at laser ignition/extinction should be avoided gradually switching on the beam

The thermo-mechanical model cannot be used as a stand-alone tool allowing for a complete planning of the SLM strategy due to its limitations in terms of domains that can be simulated. Besides, the model lacks a full experimental validation to ensure its capacity to provide reliable quantitative results. Nevertheless, considering its ability to reproduce experimentally observed main SLM mechanical phenomena, the thermo-mechanical model can be of use in a process parameter design procedure to orientate and thus speed up their optimization. Indeed, it gives insight into the effects of these parameter variations thus providing information on how they could be modified to improve the final part quality.

Acknowledgements

References

[1] E. Malekipour and H. El-Mounayri, "Common defects and contributing parameters in powder bed fusion am process and their classification for online monitoring and control: a review," *The International Journal of Advanced Manufacturing Technology*, vol. 95, no. 1, pp. 527–550, 2018.

[2] D. Buchbinder, W. Meiners, N. Pirch, K. Wissenbach, and J. Schrage, "Investigation on reducing distortion by preheating during manufacture of aluminum components using selective laser melting," *Journal of Laser Applications*, vol. 26, no. 1, p. 012004, 2014.

[3] F. Neugebauer, N. Keller, V. Ploshikhin, F. Feuerhahn, and H. Köhler, "Multi scale FEM simulation for distortion calculation in additive manufacturing of hardening stainless steel," in *Proc. Int. Workshop on Thermal forming and welding distortion, Bremen*, 2014.

[4] L. Papadakis, A. Loizou, J. Risse, and J. Schrage, "Numerical computation of component shape distortion manufactured by selective laser melting," *Proceedings of the International Conference on Manufacturing of Lightweight Components: Manulight 2014*, vol. 18, no. 0, pp. 90–95, 2014.

[5] I. A. Roberts, C. J. Wang, M. Stanford, K. A. Kibble, and D. J. Mynors, "Experimental and numerical analysis of residual stresses in additive layer manufacturing by laser melting of metal powders," in *Advanced Design and Manufacture III*, vol. 450 of *Key Engineering Materials*, pp. 461–465, Trans Tech Publications, 2011.

[6] L. Van Belle, G. Vansteenkiste, and J. C. Boyer, "Investigation of residual stresses induced during the selective laser melting process," in *16th ESAFORM Conference on Material Forming (ESAFORM 2013)*, vol. 554-557, pp. 1828–1834, Trans Tech Publications, 2013.

[7] Y. Zhang, Q. Chen, G. Guillemot, C.-A. Gandin, and M. Bellet, "Numerical modelling of fluid and solid thermomechanics in additive manufacturing by powder-bed fusion: Continuum and level set formulation applied to track- and part-scale simulations," *Comptes Rendus Mécanique*, vol. 346, no. 11, pp. 1055 – 1071, 2018.

[8] E. Salvati, A. J. Lunt, C. P. Heason, G. J. Baxter, and A. M. Korsunsky, "An analysis of fatigue failure mechanisms in an additively manufactured and shot peened in 718 nickel superalloy," *Materials & Design*, vol. 191, p. 108605, 2020.

[9] E. Salvati, A. Lunt, S. Ying, T. Sui, H. Zhang, C. Heason, G. Baxter, and A. Korsunsky, "Eigenstrain reconstruction of residual strains in an additively manufactured and shot peened nickel superalloy compressor blade," *Computer Methods in Applied Mechanics and Engineering*, vol. 320, pp. 335 – 351, 2017.

[10] A. G. Demir and B. Previtali, "Additive manufacturing of cardiovascular CoCr stents by selective laser melting," *Materials & Design*, vol. 119, pp. 338 – 350, 2017.

[11] Y. Wessarges, R. Hagemann, M. Gieseke, C. Noelke, S. Kaierle, W. Schmidt, K. P. Schmitz, and H. Haferkamp, "Additive manufacturing of vascular implants by selective laser melting," *Biomedical Engineering / Biomedizinische Technik*, vol. 59, pp. S401–S404, 10 2014.

[12] N. E. Hodge, R. M. Ferencz, and J. M. Solberg, "Implementation of a thermomechanical model for the simulation of selective laser melting," *Computational Mechanics*, vol. 54, no. 1, pp. 33–51, 2014.

[13] R. Ganeriwala, M. Strantza, W. King, B. Clausen, T. Phan, L. Levine, D. Brown, and N. Hodge, "Evaluation of a thermomechanical model for prediction of residual stress during laser powder bed fusion of Ti-6Al-4V," *Additive Manufacturing*, vol. 27, pp. 489 – 502, 2019.

[14] C. Bruna-Rosso, A. G. Demir, and B. Previtali, "Selective laser melting finite element modeling: Validation with high-speed imaging and lack of fusion defects prediction," *Materials & Design*, vol. 156, pp. 143 – 153, 2018.

[15] J. Lemaitre and J.-L. Chaboche, *Mechanics of solid materials*. Cambridge University Press, 1994.

[16] A. F. Bower, *Applied mechanics of solids*. CRC Press, 2010.

[17] R. Hill, *The mathematical theory of plasticity*, vol. 11. Oxford university press, 1998.

[18] J. C. Simo, "Algorithms for static and dynamic multiplicative plasticity that preserve the classical return mapping schemes of the infinitesimal theory," *Computer Methods in Applied Mechanics and Engineering*, vol. 99, no. 1, pp. 61 – 112, 1992.

[19] J. Bonet and R. D. Wood, *Nonlinear continuum mechanics for finite element analysis*. Cambridge university press, 1997.

[20] I. Doghri, *Mechanics of deformable solids: linear, nonlinear, analytical and computational aspects.* Springer-Verlag Berlin Heidelberg, 2000.

[21] J. C. Simo and T. J. R. Hughes, *Computational Inelasticity.* Interdisciplinary Applied Mathematics 7, Springer-Verlag New York, 1st ed., 1998.

[22] A. Ibrahimbegovic, *Nonlinear Solid Mechanics.* Solid Mechanics and its Applications 160, Springer Netherlands, 1 ed., 2009.

[23] G. A. Holzapfel, *Nonlinear Solid Mechanics: A Continuum Approach for Engineering.* Wiley, 1st ed., 2000.

[24] L. Vujosevic and V. Lubarda, "Finite-strain thermoelasticity based on multiplicative decomposition of deformation gradient," *Theoretical and Applied Mechanics*, vol. 28-29, pp. 379 – 399, 2002.

[25] J. K. Panayiotis and B. Marc-Jean, "Thermal and structural properties of fusion related materials." http://www-ferp.ucsd.edu/LIB/PROPS/PANOS/, 1997.

[26] L. Anand, "Constitutive equations for the rate-dependent deformation of metals at elevated temperatures," *Journal of engineering materials and technology*, vol. 104, no. 1, pp. 12–17, 1982.

[27] E. Voce, "A practical strain hardening function," *Metallurgia*, vol. 51, pp. 219–226, 1955.

[28] K. Singh, "Strain hardening behaviour of 316L austenitic stainless steel," *Materials Science and Technology*, vol. 20, no. 9, pp. 1134–1142, 2004.

[29] C. Bruna-Rosso, A. G. Demir, B. Previtali, and M. Vedani, "Selective laser melting high performance modeling," in *Proceedings of 6th International Conference on Additive Technologies* (I. Drstvenek, D. Drummer, and M. Schmidt, eds.), pp. 252 – 259, Interesansa - zavod, Ljubljana, 2016.

[30] J. Smith, W. Xiong, J. Cao, and W. K. Liu, "Thermodynamically consistent microstructure prediction of additively manufactured materials," *Computational Mechanics*, vol. 57, no. 3, pp. 359–370, 2016.

[31] R. Casati, J. Lemke, and M. Vedani, "Microstructure and fracture behavior of 316L austenitic stainless steel produced by selective laser melting," *Journal of Materials Science & Technology*, vol. 32, no. 8, pp. 738 – 744, 2016.

[32] C. Li and B. G. Thomas, "Thermomechanical finite-element model of shell behavior in continuous casting of steel," *Metallurgical and Materials Transactions B*, vol. 35, no. 6, pp. 1151–1172, 2004.

[33] S. Koric and B. G. Thomas, "Efficient thermo-mechanical model for solidification processes," *International Journal for Numerical Methods in Engineering*, vol. 66, no. 12, pp. 1955–1989, 2006.

[34] E. R. Denlinger, J. C. Heigel, and P. Michaleris, "Residual stress and distortion modeling of electron beam direct manufacturing Ti-6Al-4V," *Proceedings of the Institution of Mechanical Engineers, Part B: Journal of Engineering Manufacture*, 2014.

[35] H. Peng, M. Ghasri-Khouzani, S. Gong, R. Attardo, P. Ostiguy, R. Rogge, B. Aboud Gatrell, J. Budzinski, C. Tomonto, J. Neidig, M. Shankar, R. Billo, D. Go, and D. Hoelzle, "Fast prediction of thermal distortion in metal powder bed fusion additive manufacturing: Part 2, a quasi-static thermo-mechanical model," *Additive Manufacturing*, vol. 22, pp. 869–882, 2018.

[36] K.-J. Bathe, *Finite element procedures*, vol. Part 1-2. Prentice Hall, 2nd ed., 1996.

[37] S. Léger, A. Fortin, C. Tibirna, and M. Fortin, "An updated lagrangian method with error estimation and adaptive remeshing for very large deformation elasticity problems," *International Journal for Numerical Methods in Engineering*, vol. 100, no. 13, pp. 1006–1030, 2014.

[38] F. Auricchio and R. Taylor, "A return-map algorithm for general associative isotropic elasto-plastic materials in large deformation regimes," *International Journal of Plasticity*, vol. 15, no. 12, pp. 1359 – 1378, 1999.

[39] P. Mercelis and J. P. Kruth, "Residual stresses in selective laser sintering and selective laser melting," *Rapid Prototyping Journal*, vol. 12, no. 5, pp. 254–265, 2006.

[40] M. Shiomi, K. Osakada, K. Nakamura, T. Yamashita, and F. Abe, "Residual stress within metallic model made by selective laser melting process," *CIRP Annals*, vol. 53, no. 1, pp. 195 – 198, 2004.

[41] T. Simson, A. Emmel, A. Dwars, and J. Böhm, "Residual stress measurements on AISI 316L samples manufactured by selective laser melting," *Additive Manufacturing*, vol. 17, pp. 183 – 189, 2017.

[42] D. Arndt, W. Bangerth, T. C. Clevenger, D. Davydov, M. Fehling, D. Garcia-Sanchez, G. Harper, T. Heister, L. Heltai, M. Kronbichler, R. M. Kynch, M. Maier, J.-P. Pelteret, B. Turcksin, and D. Wells, "The `deal.II` library, version 9.1," *Journal of Numerical Mathematics*, vol. 27, no. 4, pp. 203–213, 2019.

[43] L. Van Belle, G. Vansteenkiste, and J. C. Boyer, "Comparisons of numerical modelling of the selective laser melting," in *15th ESAFORM Conference on Material Forming (ESAFORM 2012)*, vol. 504, pp. 1067–1072, Trans Tech Publications, 2012.

[44] B. Cheng, S. Shrestha, and K. Chou, "Stress and deformation evaluations of scanning strategy effect in selective laser melting," *Additive Manufacturing*, vol. 12, pp. 240 – 251, 2016.

[45] B. Zhang, L. Dembinski, and C. Coddet, "The study of the laser parameters and environment variables effect on mechanical properties of high compact parts elaborated by selective laser melting 316L powder," *Materials Science and Engineering: A*, vol. 584, pp. 21 – 31, 2013.

[46] R. K. Desu, H. N. Krishnamurthy, A. Balu, A. K. Gupta, and S. K. Singh, "Mechanical properties of austenitic stainless steel 304L and 316L at elevated temperatures," *Journal of Materials Research and Technology*, vol. 5, no. 1, pp. 13 – 20, 2016.

[47] J.-P. Kruth, J. Deckers, E. Yasa, and R. Wauthl, "Assessing and comparing influencing factors of residual stresses in selective laser melting using a novel analysis method," *Proceedings of the Institution of Mechanical Engineers, Part B: Journal of Engineering Manufacture*, vol. 226, no. 6, pp. 980–991, 2012.

[48] H. Yeung, B. Lane, J. Fox, F. Kim, J. Heigel, and J. Neira, "Continuous laser scan strategy for faster build speeds in laser powder bed fusion system," in *The Solid Freeform Fabrication Symposium*, 2016.

[49] U. Scipioni Bertoli, A. J. Wolfer, M. J. Matthews, J.-P. R. Delplanque, and J. M. Schoenung, "On the limitations of volumetric energy density as a design parameter for selective laser melting," *Materials & Design*, vol. 113, pp. 331 – 340, 2017.

[50] W. E. King, H. D. Barth, V. M. Castillo, G. F. Gallegos, J. W. Gibbs, D. E. Hahn, C. Kamath, and A. M. Rubenchik, "Observation of keyhole-mode laser melting in laser powder-bed fusion additive manufacturing," *Journal of Materials Processing Technology*, vol. 214, no. 12, pp. 2915 – 2925, 2014.